High Energy Physics Laboratory,
Department of Physics,
Nara Women's University,
Nara 630, JAPAN

NWU-HEP 96-01

Measurement of inclusive electron cross section in $\gamma\gamma$ collisions at TRISTAN

Masako Iwasaki

Human Life and Environmental Science Course,
Graduate School of Human Culture,
Nara Women's University
Nara 630, JAPAN

January 1996

Ph.D Dissertation

Abstract

We have studied the charm-quark production in high-energy $\gamma\gamma$ collisions with the TOPAZ detector at TRISTAN e^+e^- collider (KEK). In this study, charm quarks were identified by electrons (and positrons) from semi-leptonic decay of charmed hadrons. The data corresponded to an integrated luminosity of 95 pb^{-1} at center-of-mass energy ($\sqrt{s}$) of 58 GeV. The results are presented as cross sections of inclusive-electron production and its transverse momentum dependence. A comparison with theoretical predictions based on the Quantum Chromodynamics (QCD) showed that our data prefer that with relatively large gluon contents in a photon, with the next-to-leading order (NLO) QCD correction, and with a relatively low charm-quark mass of 1.3 GeV. On the other hand, the direct process (Quark-parton model) alone falls short of the observed inclusive-electron cross section.

Acknowledgements

The physical results presented in this thesis were obtained in the TOPAZ experiment at TRISTAN. It is my great happiness to have been able to participate in the TOPAZ collaboration. I would like to thank all of the people, physicists and engineers of the collaboration and the TRISTAN accelerator staff, who made this work possible.

I would like to thank Prof. Seishi Noguchi, Dr. Hisaki Hayashii, and Prof. Noboru Fujiwara for their continous advice and encouragement. I would like to thank all of the members of High Energy Physics Laboratory at Nara Women's University for their kind help.

Special thanks are due to Dr. Ryoji Enomoto for his patient guidance and valuable suggestions throughout the work. It must have been impossible to complete the work without his help. I would also like to thank the members of the TOPAZ two-photon working group for their useful discussions on the physics. I would like to thank all graduate students in the TOPAZ collaboration. It was my pleasure to discuss and work with them.

Finally, I would like to express my thanks to my family for their continuous encouragement and affectionate support.

Contents

List of Figures

List of Tables

Chapter 1

Introduction

In the development of the elementary particle physics, electron-positron colliders have played a major role, from the discovery of the J/ψ to the recent precise measurement of parameters of the neutral weak boson (Z^0-boson). In the electron-positron colliding, two dominant processes exist. One is the e^+e^- annihilation process where the electron and positron annihilate and produce a single virtual time-like photon or Z^0-boson, which subsequently materializes into hadrons or leptons in the final state as shown in Fig.1.1.

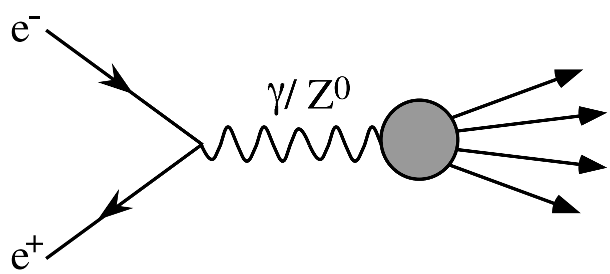

Figure 1.1: e^+e^- annihilation process.

The other is the two-photon process ($e^+e^- \rightarrow e^+e^- + X$), where two virtual space-like photons, which are emitted by beam electron and positron, interact and produce hadrons or leptons in the final state as shown in Fig.1.2. Though the cross section for the two-photon process is suppressed by α^2 ($\alpha \equiv e^2/4\pi \simeq 1/137$) compared to the e^+e^- annihilation process of Fig.1.1, the radiation of a photon leads to a characteristic double bremsstrahlung factor of $\ln^2(E_{beam}^2/m_e^2)$, which becomes significantly large at sufficiently high energies. Thus the two-photon processes become increasingly important at higher energy e^+e^- colliders, and can

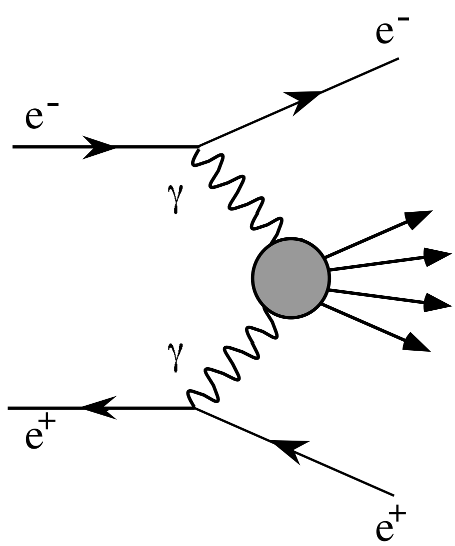

Figure 1.2: Two-photon process in $e^+e^- \rightarrow e^+e^- + X$.

be used to study the several aspects of the properties of high-energy photon.

The photon is the simplest of all bosons. It is the gauge boson of QED, which implies that it is massless and structureless (i.e. pointlike). The predictions of QED for purely leptonic processes can be made with impressive accuracy, in some cases (e.g. g-2 experiments[1]) to better than 10^{-8}. This is a great success of the Quantum Field Theories in general.

However, many reactions involving the (almost-) real photons, such as real photon-photon ($\gamma\gamma$), virtual and real photon ($\gamma^*\gamma$), and real photon and proton (γp) collisions, are much less understood both experimentally and theoretically. In these reactions, it has been known that the (almost-) real photon behaves as a composite object like a hadron, as well as a pointlike object.

Theoretically, this dual (i.e. pointlike and hadronic) nature of the photon can be understood qualitatively that the photon fluctuate into a pair of charged particles for short time. Fluctuations into virtual two-lepton states are well understood by QED, however, fluctuations into quark-antiquark pairs are much more complicated. It is a subject of Quantum Chromodynamics (QCD).* The complicated hadronic state of (almost-) real photon can be evolved from a (virtual) $q\bar{q}$ state

*QCD describes the strong force between quarks and (anti-) quarks by exchanging the spin-1 bosons, called gluons. The source of this force is the color charge. Quarks carry three kinds of colors, red (R), green (G), and blue (B) and gluons also carry bi-colors such as R$\bar{\text{B}}$. Since a gluon carries bi-colors, it can couple with each other. Due to the gluon self-coupling, the effective coupling strength of the strong interaction $\alpha_s(Q^2)$ decreases logarithmically as Q^2 increases. In whenever the life-time of the virtual $q\bar{q}$ state exceeds about 10^{-25} sec which corresponds to a characteristic energy scale below about 1 GeV or less. It cannot be described by perturbative methods alone. Even if the energy scale is larger, hard-gluon emissions and the related processes complicate the nature of the photon substantially.

The dual nature of the photon leads to rich phenomena in real $\gamma\gamma$ collisions. Examples of diagrams contributing to the hadron production in real $\gamma\gamma$ collisions in e^+e^- experiments are shown in Figs. 1.3. Historically, only first two diagrams; (a) the direct-photon process; and (b) the vector-meson dominance model (VDM) process[2], have been taken into account for the experimental analysis. In the direct process, photons couple to quarks directly and produce quark anti-quark pairs at large angles having high-transverse momentum (P_T). The quarks are then hadronized into ordinary hadrons such as π, K $\cdots$ mesons. If the momentum is large enough, jet-like structure (a collimated flow of hadrons) might be observed in the final state. On the other hand, in the VDM process, the photon is treated as a vector-meson ($\rho, \omega, \phi \cdots$) which has the same quantum number as that of the photon. The final hadronic state in this process has relatively low-P_T. However, this process is out of scope of the perturbative-QCD theory.

Recently, the existence of another important classes of the diagrams which contribute to $\gamma\gamma$ collisions, as shown in Fig. 1.3 (c) and (d), were proposed[3-5]. Following the notation in Ref. [3], we call them "resolved"-photon processes since one or both of photons are "resolved" into their hadronic constituents, i.e. quark and gluon. If only one photon is resolved into its partonic components, and interacts with the other photon as shown in Fig. 1.3 (c), the process is called "one-resolved" process. On the other hand, the process where both photons are resolved into their partonic constituents is called "two-resolved" process; an example is shown in Fig.1-3(d). The prediction of cross sections for the resolved-photon processes can be given by a perturbative-QCD. The basic formula of the resolved-

---

the leading-order (LO), it can be written as

$$\alpha_s(Q^2) = \frac{12\pi}{(33 - 2n_f)\ln Q^2/\Lambda^2},$$

where n_f is the number of flavors relevant to the reaction, Λ is the QCD scale parameter, and Q^2 is a typical energy scale of the reaction. In other words, quarks interact weakly at sufficient high energy (short distance), but interact strongly at low energy (long distance). This is the most striking feature of QCD and is called the asymptotic freedom. The phenomena at high energy can be calculated with QCD where α_s is sufficiently small to use perturbative methods. However the low-energy phenomena, such as bound states of quarks (i.e. hadrons) can not be treated by perturbative methods.

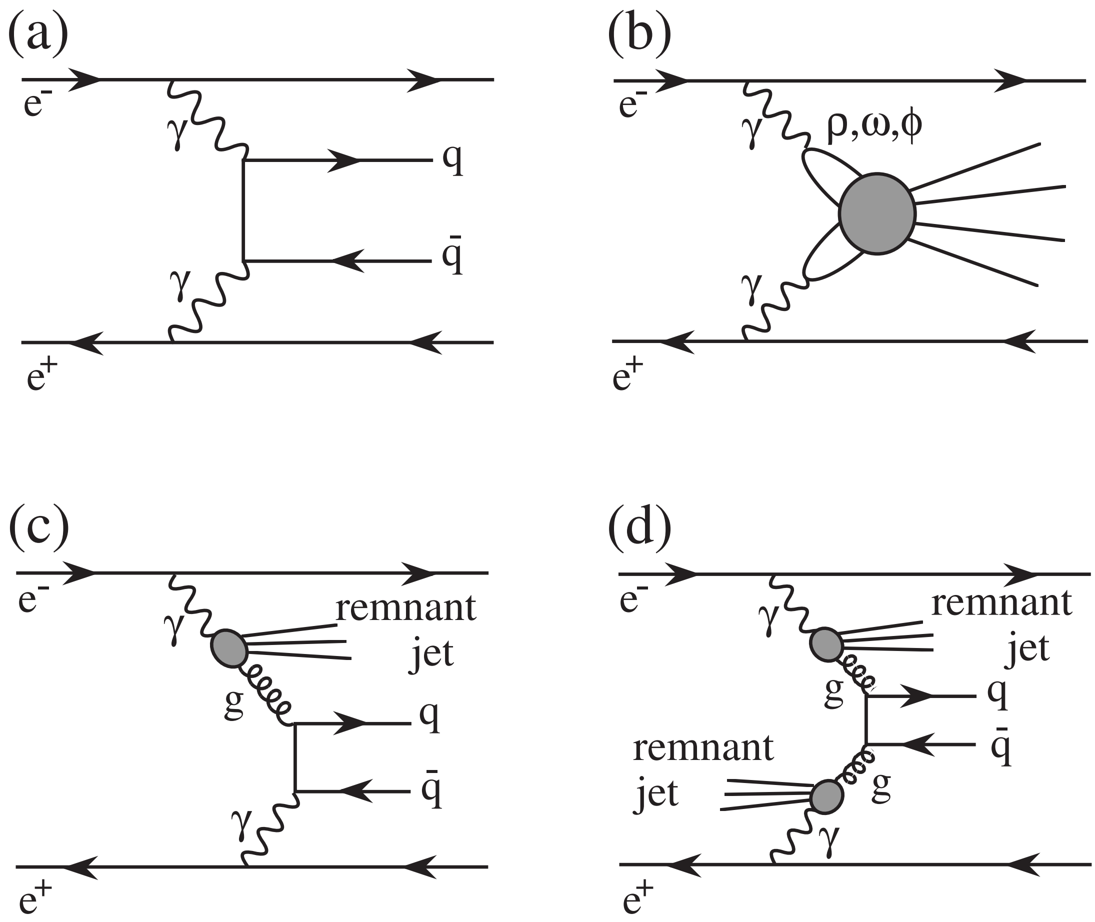

Figure 1.3: Examples of Feynman diagrams contributing to the hadron production in real $\gamma\gamma$ collisions in e^+e^- experiments: (a) direct (QPM) process, (b) VDM process, (c) one-resolved-photon process, and (d) two-resolved process.

photon process is very similar to that used in the high-P_T jet production in hadron-hadron (pp, $p\bar{p}$) collisions. In these hadron-hadron collisions, if P_T of the final-state jets are large enough, partons inside the hadron can be treated as quasi-free particles, because of the asymptotic free nature of the strong force. The jet cross section is given as a convolution of the parton distribution in the hadron (i.e. the structure function of the hadron) and the cross section of the parton-parton scattering. Similarly, it is possible to define the parton distribution inside the photon. This parton distribution in the photon is an important parameter to describe the hadron production in many reactions which involve real photons.

Predicted cross sections for the one-resolved and two-resolved processes are the same order as that for the direct process at the TRISTAN energy region, and increase rapidly with increasing of the beam energy. Thus to understand these reactions is important for the future high-energy e^+e^- colliders. In addition to the magnitude of the cross section, another distinct feature of the resolved-photon process is the existence of the remnant-jets originating from remaining constituents in the photon. These remnant components might be produced predominantly along the beam direction.

In the previous experiments carried out at the PEP and the PETRA e^+e^- colliders[6-8], the data of the hadron production in $\gamma\gamma$ collisions were compared to only the direct and VDM contributions. Although the reason was not well understood, a significant excess of the data over the direct and VDM predictions was already observed. The existence of the resolved-photon processes was first confirmed by the AMY group at TRISTAN[9]. They showed the data on multi-hadron production in $\gamma\gamma$ collisions which could be reproduced by the prediction based on the resolved-photon process. However, this early experiment of the multi-hadron production in $\gamma\gamma$ collisions was not possible to compare to theoretical predictions directly. The production of actual reconstructed jets (using a cone algorithm) has been studied recently, first by the TOPAZ group[10] and then by the AMY group[11]. The TOPAZ group also reported an evidence for the associated remnant-jet activity in the small-angle detectors. Fig. 1.4 shows the presented distribution of the particle energy flow for the sample which has two high-P_T jets in the central region. In this figure, large activities are clearly observed in the small-angle region ($0.972 < |\cos\theta| < 0.9984$). The evidence for the resolved-photon processes and its remnant-jets were also observed in γp collisions at HERA[12].

These data on jet production have provided us with some important information about the quark and gluon contents of the photon: the experimental

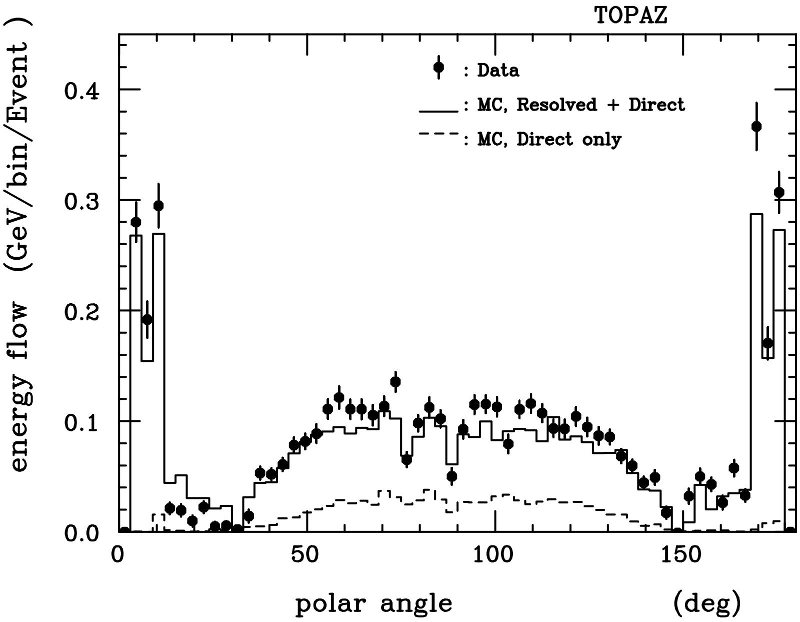

Figure 1.4: Maximum cluster-energy distribution measured with the calorimeters in the polar angular region of $0.895 < |\cos\theta| < 0.9984$ for the sample which has two high-P_T jets in the central region ($|\eta_{jet}| < 0.7$). Experimental data (closed circle) are compared with the theoretical prediction based on the direct process only (dot-dashed histogram) and that based on the direct + resolved-photon process (solid histogram). The VDM contribution is negligible for this sample.

data of the inclusive jet cross section are not consistent with a very hard gluon distribution(LAC3[13]), as clearly shown in Fig. 1.5. However, the sensitivity of the data was limited to high Bjorken-$x^\dagger$ values ($x > 0.1$) because of the experimental P_T cut applied in jet reconstruction and a theoretical cut (P_T^{min}) in order to justify the perturbative-QCD calculation.

Charm-quark production in $\gamma\gamma$ collisions is a good tool for studying the parton-production mechanisms in two-photon processes[14]. The reaction has several advantages over light-quark production. Their heavy mass $m_Q \gg \Lambda_{QCD}$ ensures the QCD perturbation theory to be applicable at almost whole phase space. The total cross-section therefore can be predicted without the cut-off parameter P_T^{min} which was introduced to justify the perturbative-QCD calculation in light-quark production. The dominant mechanisms for the charm-quark production are only the direct process $\gamma\gamma \to Q\bar{Q}$ and the one-resolved process $\gamma g \to Q\bar{Q}$ (photon-gluon fusion), because the contribution of the two-resolved process $gg \to Q\bar{Q}$ or $q\bar{q} \to Q\bar{Q}$ is considered to be negligibly small at the TRISTAN energy region. Charmed-hadron production from the VDM process is also expected to be negligible. Higher order QCD corrections ($O(\alpha_s)$) are available for both the direct and the one-

†Bjorken-x is defined as the momentum fraction of the parton divided from the parent photon.

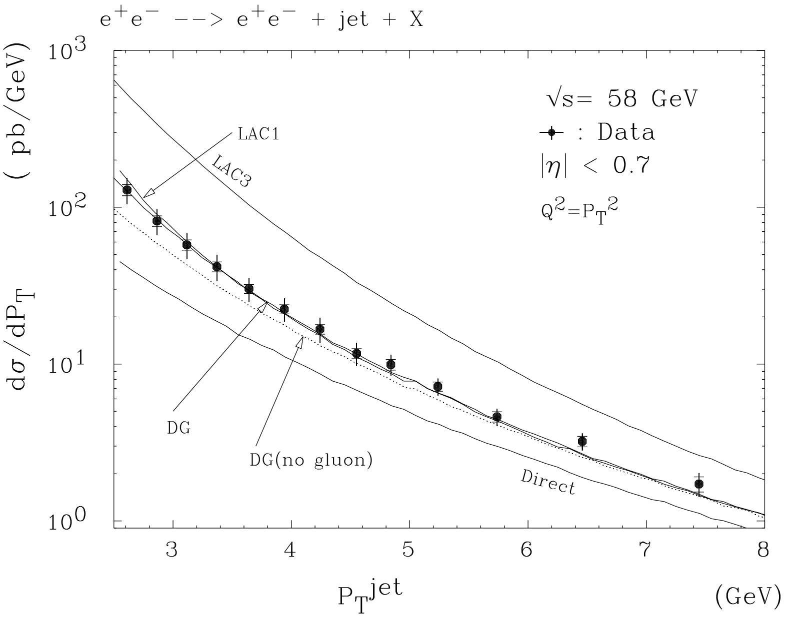

Figure 1.5: Inclusive jet cross section as a function of the P_T of jet for the pseudo-rapidity interval $|\eta_{jet}| < 0.7$. Closed circles indicates the experimental data. The dashed line shows the prediction of the direct process. The various predictions based on the direct + resolved-photon processes are also plotted.

resolved processes[14]. Studies of charm production in $\gamma\gamma$ collisions thus provide a good opportunity to probe the gluon density in the photon. From the previous experiments, little is known for the gluon density in the photon though it is the important parameter as described in the next chapter.

In the PEP/PETRA experiments[15] and the previous TRISTAN experiments[16, 17], charm quarks were identified by detecting $D^{*\pm}$ signals. In this thesis, we use electrons and positrons in the final states to tag charm-quark production in $\gamma\gamma$ collisions (hereafter, positron is also expressed as electron). The same kind of inclusive-election analysis was carried out by the VENUS group[18], but it had low statistics and did not give any cross sections.

Comparing to the $D^{*\pm}$ method, the electron method has several advantages. This method is sensitive to the charm-quark production at low-P_T, where the one-resolved process contributes significantly. This kinematical region corresponds to the small-x region where model dependence is the largest among various parametrization of the gluon density in the photon[13, 19-23]. In this analysis, we can probe small-x region down to $\sim$ 0.02. In addition, since the charm quark has a large semi-leptonic branching fraction ($\sim$ 10 %)‡, high-statistics experiments can be carried out.

‡The branching fraction for the mode $D^{\pm} \rightarrow e^{\pm} + X$ and $D^0 \rightarrow e^{\pm} + X$ are 17.2 $\pm$ 1.9 % and 7.7 $\pm$ 1.2 %, respectively[24].

The organization of this thesis is as follows; Chapter 2 reviews the general formalism of light-quark production in the two-photon processes and that of heavy-quark production including the QCD corrections and the available theoretical predictions of the photon-structure functions. Chapter 3 describes the experimental apparatus of the TRISTAN accelerator and the TOPAZ detector. The trigger system and data acquisition systems are also described here. In Chapter 4, we refer to the method of the raw-data processing. In particular, the method of the particle identification is described in detail since it is crucial in this analysis. Chapter 5 describes the Monte-Carlo simulation. We then present the experimental results in Chapter 6 and 7, and discuss them in Chapter 8. Finally, the conclusions are given in Chapter 9.

Chapter 2

Hadron production in two-photon process

As described in Chapter 1, the open-charm production in $\gamma\gamma$ collisions was studied using the two-photon process ($e^+e^- \rightarrow e^+e^-$ hadrons) where two photons emitted from electron and positron scatter to produce hadrons at final state. In this chapter, we first summarize the kinematics of the reaction and then introduce the theoretical formulae of the hadron production in the two-photon processes. Finally, several theoretical treatments of the c-quark production based on QCD are reviewed.

2.1 Kinematics for two-photon process

Fig. 2.1 represents the definitions of the kinematic variables for the two-photon process. These variables in this figure are summarized in Table 2.1.

Since the photon propagator naturally peaks at $q_i^2 = 0$, the majority of events involve *almost* real photons. In this case, the scattered beam electrons and positrons remain close to incident direction and are not detected. Two-photon events can be distinguished by whether either one or both the scattered leptons is detected when θ_i is large. We call the detected electron "tagged" electron. When neither is detected, we call it "anti-tagged" events which form the major part of the two-photon data. If we do not see whether the scattered electron to be detected or not, we call them "no-tagged" events. In the anti-tag case both photons are ensured to be nearly real, however, when one (or two) scattered lepton is tagged, one (two) of the photon must be highly virtual.

For anti-tagged events, the reaction $e^+e^- \rightarrow (e^+e^-)X$ is factorized by following

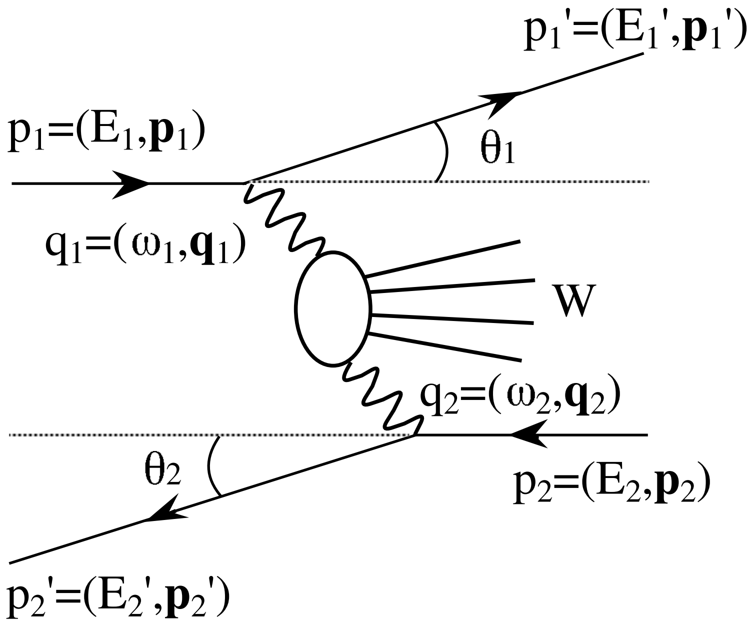

Figure 2.1: Kinematics for the two-photon process.

Variable	Description
$p_i = (E_i, \boldsymbol{p}_i)$	energy-momentum 4-vector of incident electrons
$p'_i = (E'_i, \boldsymbol{p}'_i)$	energy-momentum 4-vector of scattered electrons
$q_i = (\omega_i, \boldsymbol{q}_i)$	the 4-momentum of the virtual photon i
P_i^2	negative invariant mass squared of virtual photon $P_i^2 \equiv -q_i^2 = \boldsymbol{q}_i^2 - \omega_i^2$
W	$\gamma\gamma$ c.m. energy (i.e. $\omega_1 + \omega_2$ in the $\gamma\gamma$ c.m. frame)
θ_i	scattering angle of a scattered electron in the e^+e^- c.m. frame

Table 2.1: Kinematic variables of Fig. 2.1.

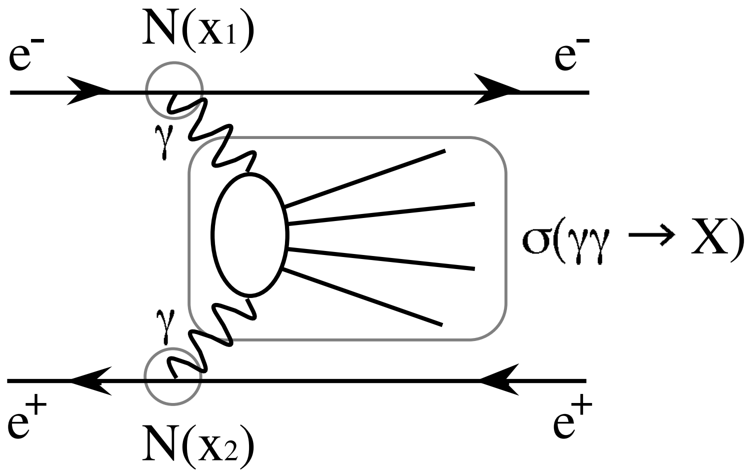

Figure 2.2: Feynman diagram for the reaction $e^+e^- \to (e^+e^-)X$.

two steps;

$$e^+e^- \to (e^+e^-)\gamma\gamma \to (e^+e^-)X.$$

In the first step, incident leptons emit quasi-real photons, and then these photons collide each other. In the next step of $\gamma\gamma \to X$, colliding two photons produce the final state X. Then the total cross section is obtained as the convolution of the photon flux $N(x_1)$ which is the probability of finding a photon of energy fraction of $x_1 = \omega_1/E_1$ and $N(x_2)$ with energy fraction x_2 times the $\gamma\gamma \to X$ cross section;

$$\sigma(e^+e^- \to (e^+e^-)X) \sim \int \sigma(\gamma\gamma \to X)N(x_1)N(x_2)dx_1dx_2,$$

as shown in the Fig. 2.2.

2.2 Cross section for two-photon process

As described in Chapter 1, three different components, i.e., VDM, direct and resolved-photon processes contribute to hadron production in the real $\gamma\gamma$ collisions. The direct and the resolved-photon processes are described with the perturbative QCD theory. While soft component of VDM is based on the phenomenological model.

2.2.1 Direct and resolved-photon processes

The general expression of the differential cross section for the direct and the resolved-photon processes is given as follows[3]:

$$\begin{aligned}\frac{d\sigma}{dP_T} &= f_{\gamma/e^-}(Q^2, x_1)dx_1 f_{\gamma/e^+}(Q^2, x_2)dx_2 \\ &\qquad q^\gamma(Q^2, x_3)dx_3 q^\gamma(Q^2, x_4)dx_4 \frac{d\hat{\sigma}(\hat{s}, \hat{t}, \hat{u})}{dP_T}. \qquad (2.1)\end{aligned}$$

The above expression is obtained by applying the equivalent real-photon approximation (EPA) to the nearly on-shell virtual photons emitted by the beam electrons[25]. Here $\hat{s} = x_1x_2x_3x_4s$ ($\sqrt{s} = 2E_{beam}$) is the squared invariant energy going into the hard sub-processes which are described by the cross section $\hat{\sigma}$. The $f_{\gamma/e^\pm}$ are the photon flux factors which represent the number of photons carrying a fraction x_i ($i = 1, 2$) of the energy of the beam electrons $e^\pm$. The q^γ is the parton (quark and gluon) density function inside the photon. As will be described later, there exist several proposed parametrization for the density function because of the large ambiguity of the gluon density. Q^2 is a relevant energy scale parameter. We chose $Q^2 = P_T^2$ for light-quark productions and $Q^2 = P_T^2 + m_c^2$ for c-quark productions[23], where P_T is the transverse momentum of the parton in the final states.

The given form of eq. 2.1 is valid for two-resolved process. The relevant diagram with the terms in eq. 2.1 is shown in Fig. 2.3. For the direct process, both q^γ in eq. 2.1 have to be replaced by $\delta(1 - x_i)$ (i=3 and 4). In this case, the sub-process is $\gamma\gamma \to q\bar{q}$. For the one-resolved process, either $q^\gamma(Q^2, x_3)$ or $q^\gamma(Q^2, x_4)$ is replaced by $\delta(1 - x_i)$. The sub-processes involved are $\gamma q \to gq$, and $\gamma g \to q\bar{q}$. There are eight sub-processes in the two-resolved process. The relevant subprocess cross sections are summarized in appendix A.

The total cross section is obtained by integrating the above formula over the kinematical P_T-region of $P_T > P_T^{min}$, where P_T^{min} is a free parameter which is introduced in order to avoid the doubly counting the soft VDM contribution and to ensure the validity of the perturbative calculation. This parameter is determined experimentally.

Photon flux

In the equivalent real-photon approximation(EPA), the photon flux factor can be written as[22, 25-27]

$$f_{\gamma/e}(x_\gamma) = \frac{\alpha_{em}}{2\pi x_\gamma}\left(1 + (1 - x_\gamma)^2\right) \ln \frac{P_{max}^2}{P_{min}^2} - \frac{\alpha_{em}}{\pi}\frac{1 - x_\gamma}{x_\gamma}, \qquad (2.2)$$

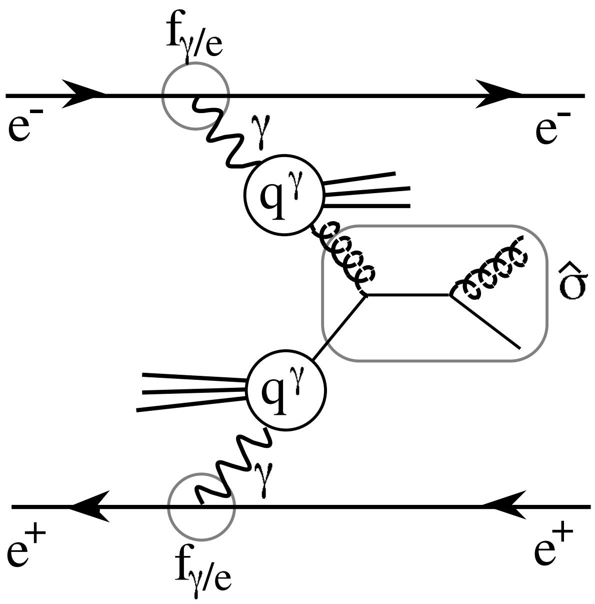

Figure 2.3: Feynman diagram for the two-resolved process.

where

$$P^2_{min} \quad = \quad m_e^2 \frac{x_\gamma^2}{1 - x_\gamma}. \tag{2.3}$$

Here, P^2_{min} is the kinematical minimum of the photon virtuality. P^2_{max} is given by

$$P^2_{max} = min(P^2_{max,kin}, Q^2), \tag{2.4}$$

where $P^2_{max,kin} = 2E^2_{beam}(1 - x_\gamma)(1 - \cos\theta_{max})$ is the maximum photon virtuality determined by the experimental anti-tag condition. Q^2 is a typical scale of the reaction which is determined by the dynamical condition that the cross section is damped for highly virtual photons. In this experiment, the scattering angles of the beam electrons were limited to less than 3.2° if their energies were greater than 0.4 E_{beam}(i.e. $\theta_{max} = 3.2°$ for $x_\gamma = E_\gamma/E_{beam} < 0.6$). P^2_{max} was mainly determined by this anti-tag condition. To check the validity of the approximation, the EPA prediction was compared with the exact matrix element calculation[28] for the direct $e^+e^- \to e^+e^-c\bar{c}$ process. We found that both predictions agree at a 1% level under this anti-tag condition[23]. The comparison of various calculations are shown in Fig. 2.4.

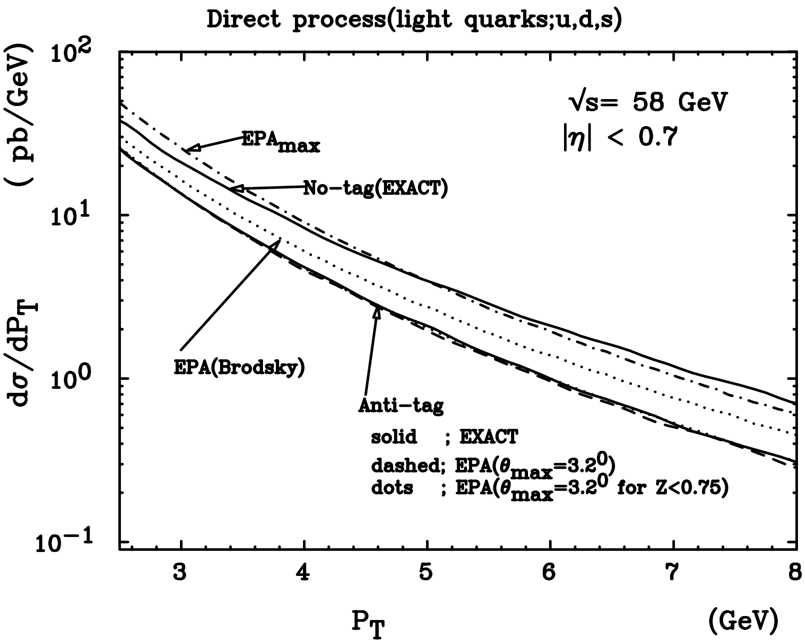

Figure 2.4: Comparison of the cross section between EPA approximation and exact matrix-element calculation in the direct-process.

Parton density function inside the photon

In QCD, the parton density inside a photon was determined by Altareli-Palisi equation (APE). The coefficients in the equation are determined by the measured photon structure function F_2^γ in deep inelastic electron-photon scattering, where F_2^γ is used for a input distribution at some scale $Q^2 = Q_0^2$.

In the deep inelastic $e\gamma$ scattering, the virtual photon γ^* emitted from tagged electron can act as a point-like probe and test the quark contents in the quasi-real target photon γ (shown in Fig. 2.5). Figs. 2.6 show the contributing diagrams to $\gamma^*\gamma$ scattering, corresponding to the blob in Fig. 2.5. Where the flavour non-singlet (NS) sector and singlet sector are treated separately. As shown in Fig. 2.6(d), there exist the nonperturbative contributions described by VDM.

According to the approach suggested by Glück and Reya [29], by summing the contributions of Figs. 2.6(a)-(d) into the single diagram of Fig. 2.6(e), the F_2^γ is expressed by the quark densities in the photon $q_i^\gamma(x, Q^2)$ as (in LO);

$$F_2^\gamma(x, Q^2) = 2x \sum_i e_{q_i}^2 q_i^\gamma(x, Q^2). \tag{2.5}$$

Where the sum runs over flavors, e_{q_i} is the electric charge of quark q_i, and the factor of 2 takes care of antiquarks. In this approach, the absolute magnitude

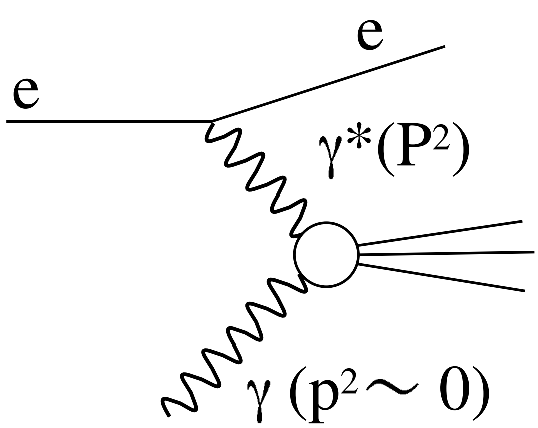

Figure 2.5: Generic Feynman diagram for deep-inelastic $e\gamma$ scattering: A probing photon with large virtuality $P^2 \equiv -q^2$ scatters off the (quasi-)real target photon (with virtuality $p^2 \simeq 0$) to produce a hadronic final state.

of the quark densities in the photon is not computed, but input distribution functions $q^\gamma_{i,0}(x) \equiv q^\gamma_i(x, Q_0^2)$ at some scale Q_0^2 are introduced. This scale is in principle arbitrary, as long as $\alpha_s(Q_0^2)$ is sufficiently small to allow a meaningful perturbative expansion.

With given these input distributions, the photonic parton densities, and thus F_2^γ, at different values of Q^2 can be computed using the inhomogeneous evolution equations. In LO, they read [30]:

$$\frac{dq^\gamma_{\rm NS}(x,Q^2)}{d\log Q^2} = \frac{\alpha_{\rm em}}{2\pi}k^\gamma_{\rm NS}(x) + \frac{\alpha_s(Q^2)}{2\pi}\left(P_{qq}\otimes q^\gamma_{\rm NS}\right)(x,Q^2); \tag{2.6}$$

$$\frac{d\Sigma^\gamma(x,Q^2)}{d\log Q^2} = \frac{\alpha_{\rm em}}{2\pi}k^\gamma_{\Sigma}(x) + \frac{\alpha_s(Q^2)}{2\pi}\Big[\left(P_{qq}\otimes \Sigma^\gamma\right)(x,Q^2) + \left(P_{qG}\otimes G^\gamma\right)(x,Q^2)\Big]; \tag{2.7}$$

$$\frac{dG^\gamma(x,Q^2)}{d\log Q^2} = \frac{\alpha_s(Q^2)}{2\pi}\Big[\left(P_{Gq}\otimes \Sigma^\gamma\right)(x,Q^2) + \left(P_{GG}\otimes G^\gamma\right)(x,Q^2)\Big], \tag{2.8}$$

where $P\otimes q$ is a convolution integral defined as,

$$\left(P\otimes q\right)(x,Q^2) \equiv \int_x^1 \frac{dy}{y}P(y)q(\frac{x}{y},Q^2). \tag{2.9}$$

$P_{ij}(y)$ is the (LO) $j \rightarrow i$ splitting function, which represents the probability that the daughter parton i carries a fraction y of the momentum of the parent parton j[31]. The explicit formulae of the splitting functions are summarized in appendix

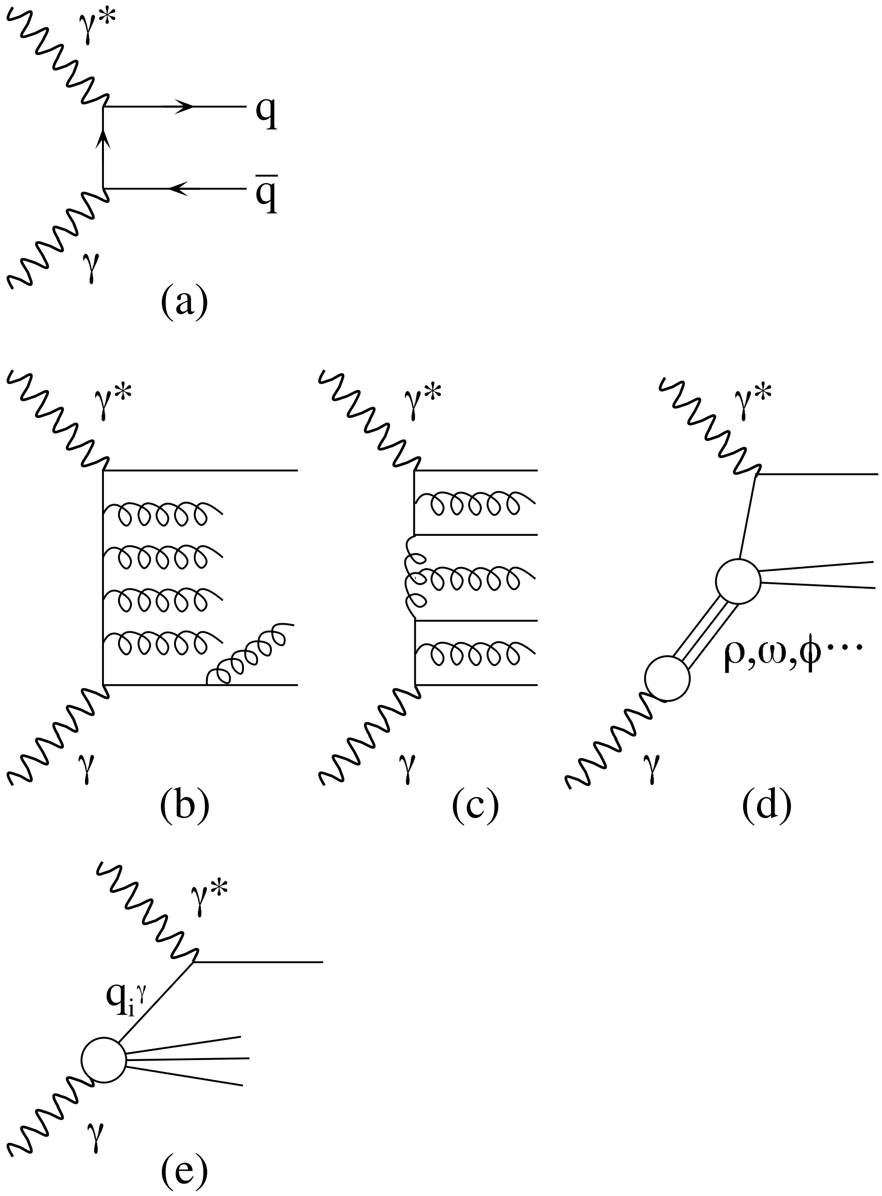

Figure 2.6: Feynman diagrams that contribute to $\gamma^*\gamma$ scattering. (a) a lowest order (QPM) contribution, (b) and (c) are examples of perturbative QCD corrections in the flavour non-singlet and singlet sector, respectively, and (d) nonperturbative contributions described by the VDM. All these contributions are formally summed in (e).

B. The inhomogeneous terms k_i^γ describe $\gamma \to q\bar{q}$ splitting, i.e. the diagram of Fig. 2.6(a), and for one quark flavour, one has

$$k_{q_i}^\gamma(x) = 3e_{q_i}^2 \left[x^2 + (1-x)^2\right]. \tag{2.10}$$

Eq.(2.6) describes the evolution of the non-singlet distributions, i.e. resume only the type of the diagrams shown in Fig. 2.6(b). While eqs.(2.7,2.8) describe the evolution of the singlet sector ($\Sigma^\gamma \equiv \sum_i q_i^\gamma + \bar{q}_i^\gamma$), which includes the diagrams of the kind shown in Fig. 2.6(c). In this sector, it is necessary to introduce a gluon density inside the photon $G^\gamma(x,Q^2)$, with its corresponding input distribution $G_0^\gamma(x) \equiv G^\gamma(x,Q_0^2)$.

From above equations, by introducing a priori unknown input distributions, it is possible to make an absolute prediction of $F_2^\gamma(x,Q^2)$ in terms of $\Lambda_{\rm QCD}$ alone. Experimental measurements of F_2^γ provide the most reliable constraints to the input distributions $\vec{q}_0^{\,\gamma}(x) \equiv (q_{i,0}^\gamma(x), G_0^\gamma(x))$ at a fixed $Q^2 = Q_0^2$. They are the only data that construct the existing parametrization of $\vec{q}^{\,\gamma}(x,Q^2)$. However, due to rather large experimental errors of data on F_2^γ, additional *assumptions* always had to be made. In addition, F_2^γ is not so sensitive to its gluon component. Several parametrization have been proposed.

The Drees-Grassie (DG) parametrization[19] was the first attempt started from the input distributions. They used a single measurement of F_2^γ at fixed $Q^2 \simeq$ 5.9 GeV^2 by PLUTO, which only existed at the time. In order to determine three independent input distributions, for non-singlet and singlet quarks as well as gluons, two assumptions were made: All input quark densities were assumed to be proportional to the squared quark charges, i.e. $u^\gamma = 4d^\gamma = 4s^\gamma$ at $Q_0^2 = 1$ GeV^2; and the gluon input was generated radiatively, i.e.

$$G_{0,\rm DG}^\gamma = \frac{2}{\beta_0}\Sigma_{0,\rm DG}^\gamma \otimes P_{Gq}, \tag{2.11}$$

where $\beta_0 = 9$ is the coefficient of the one-loop QCD β function. For the QCD scale parameter, they assumed $\Lambda_{\rm QCD} = 0.4$ GeV. This parametrization only exists in LO. Moreover, it treats flavour thresholds by introducing three independent sets of distributions for $N_f = 3,\ 4,\ 5$, so that the transition across a threshold is not smooth.

The Levy-Abramowicz-Charchula (LAC) parametrization[13] are based on a much larger data set. The obtained three solutions which depend on the Q_0^2 values ($Q_0^2 = 4.0$ GeV for LAC1 and LAC2 , and $Q_0^2 = 1.0$ GeV for LAC3) and the treatment of the gluon density. In this parametrization, $\Lambda_{\rm QCD}$ was assumed to be 0.2 GeV. The main point of these fits was to demonstrate that the data on F_2^γ

constrain G^γ very poorly. In particular, they allow a very hard gluon, with xG^γ having a maximum at $x \simeq 0.9$ (LAC3), as well as very soft gluon distributions, with xG^γ rising very steeply at low x (LAC1, LAC2). The LAC parametrization only exist for $N_f = 4$ massless flavors and in LO. *No* assumptions about the relative sizes of the four input quark densities were made in the fit.

The Watanabe-Hagiwara-Izubuchi-Tanaka (WHIT) parametrization [23] follow a similar philosophy as LAC, at least regarding the gluon input. In the WHIT1,2,3 parametrization, gluons are assumed to carry about half of the photon's momentum as quarks do (at the input scale $Q_0^2 = 4$ GeV^2), while in WHIT4,5,6 gluons and quarks carry about the same momentum fraction. These two groups of fits also have slightly different valence quark densities. The input gluon density is assumed to have the simple shape $xG_0^\gamma \propto (1-x)^{c_g}$, with $c_g = 3$ for WHIT1,4; $c_g = 9$ for WHIT2,5; and $c_g = 15$ for WHIT3,6. The WHIT parametrization only exists in LO, but they treated the ($x-$dependent) charm threshold correctly.

Figs. 2.7 show the comparison of (a) F_2^γ and (b) gluon density with each other at the same value of Q^2. The F_2^γ are well constrained by experiments. While, obviously the parametrization for the gluon densities differ much more than that for the quark densities determined by F_2^γ.

The LAC3 parametrization, which has very hard gluon distribution among the parametrization, was clearly excluded from the experiment in real $\gamma\gamma$ scattering[10] as well as in ep scattering. The other parametrization differ especially at low-x region. The gluon distribution of LAC1/WHIT4 increases more rapidly than that of DG/WHIT1 at x less than 0.1.

2.2.2 VDM process

The cross section for VDM is given by;

$$\sigma^{VDM} = \int f_{\gamma/e^-}(x_1) f_{\gamma/e^+}(x_2) \sigma_{\gamma\gamma}^{VDM} dx_1 dx_2. \tag{2.12}$$

Where $\sigma_{\gamma\gamma}^{VDM}$ denotes the cross section of the $\gamma\gamma$ collision in VDM, which expressed in a factorized form of;

$$\sigma_{\gamma\gamma}^{VDM} = \sigma(W^2) \cdot F(Q_1^2) \cdot F(Q_2^2). \tag{2.13}$$

For the form factor $F(Q^2)$, we used the Generalized VDM form[2]. Since $F(Q^2) = 1$ at $Q^2 = 0$, the factor $\sigma(W^2)$ become the total $\gamma\gamma$ cross section when γ is real. According to the previous measurements by PLUTO[32], CELLO[8], and

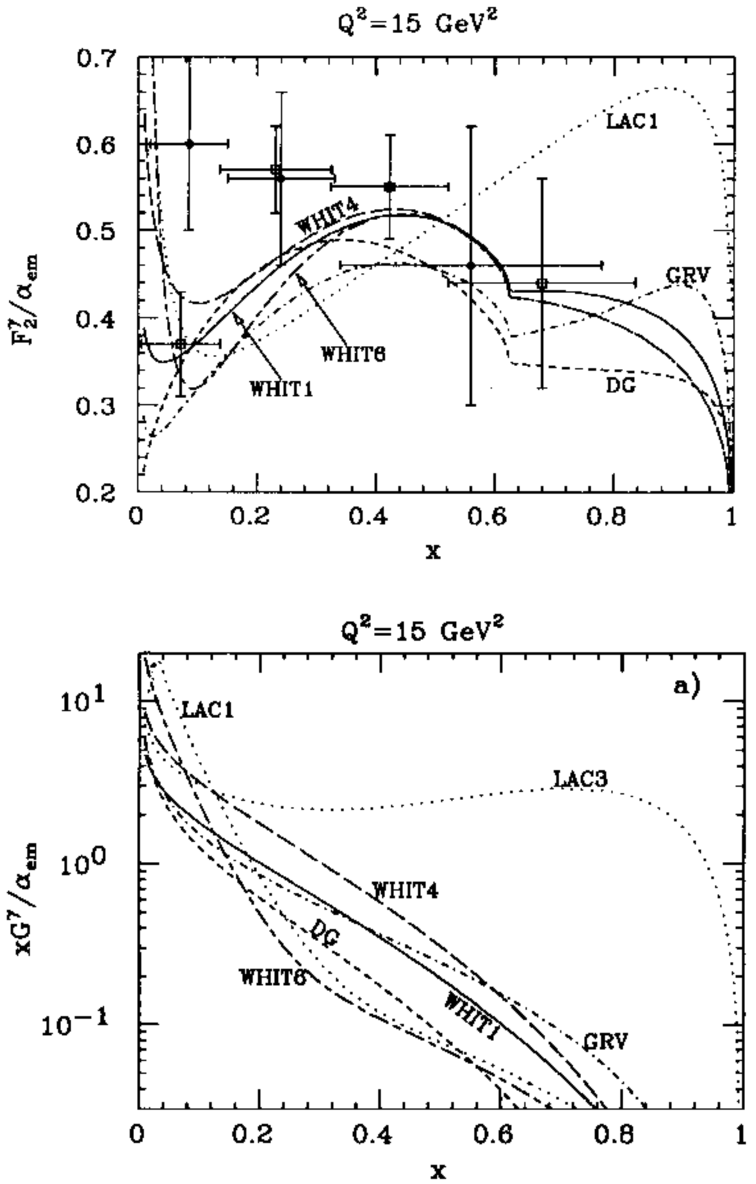

Figure 2.7: Predictions of various existing parametrization of photonic parton densities (a) for the structure function F_2^γ at $Q^2 = 15$ GeV and (b) for the gluon content in the photon at $Q^2 = 15$ GeV.

TPC/2γ[7], the $\sigma(W^2)$ seemed approximately independent of W, and the values were in the ranges from 200 nb to 420 nb. In this analysis, we used the form $\sigma(W) = 240+270/W$ (nb), given by Rosner[33]. The final state hadron is assumed to be the exponential form, that is;

$$\frac{d\sigma}{dP_T^2} \sim \exp(-\alpha P_T^2). \tag{2.14}$$

The slope parameter α was in the range of $2 \leq \alpha \leq 5$ GeV^{-2}. We set the value to be 4.0 GeV^{-2}.

2.3 Open-charm production

As described earlier, heavy quark (open-charm) production is a good tool for studying the two-photon process. Since it is a hard QCD process, it is expected that the VDM contribution is negligible and the cut off parameter P_T^{min} is unnecessary. The theoretical uncertainly is therefore considered to be less than the light-quark productions. The generic diagrams for the heavy quark productions are shown in Figs. 2.8; (A) direct process, (B) one-resolved process, and (C) two-resolved process.

A. Direct process

In the direct process, the cross section at Born level (A1) is given by[34],

$$\sigma_0(\gamma\gamma \to Q\bar{Q}) = \frac{4\pi\alpha^2 e_Q^4 N_c}{s_{\gamma\gamma}} \left[\left(1 + \frac{4m_Q^2}{s_{\gamma\gamma}} - \frac{8m_Q^4}{s_{\gamma\gamma}^2} \right) \log\frac{1+\beta}{1-\beta} - \beta\left(1 + \frac{4m_Q^2}{s_{\gamma\gamma}} \right) \right], \tag{2.15}$$

where $s_{\gamma\gamma}$ denotes the total $\gamma\gamma$ energy squared and $\beta = (1 - 4m_Q^2/s_{\gamma\gamma})^{1/2}$ the velocity of the quark Q.

The cross section including the QCD corrections, virtual plus soft gluon correction (A2) and hard gluon radiation (A3), can be determined analytically[14],

$$\sigma_0(\gamma\gamma \to Q\bar{Q}(g)) = \frac{4\pi\alpha^2 e_Q^4 N_c}{s_{\gamma\gamma}}\beta \left\{ 1 + \frac{4\alpha_s}{3\pi}\left[\frac{\pi^2}{2\beta} - \left(5 - \frac{\pi^2}{4} \right) + O(\beta) \right] \right\}. \tag{2.16}$$

The predictions for the direct process only depend on the heavy-quark mass and QCD coupling constant α_s. The final result can be summarized in the form

$$\sigma(\gamma\gamma \to Q\bar{Q}(g)) = \frac{\alpha^2 e_Q^4}{m_Q^2} \left(c_{\gamma\gamma}^{(0)} + 4\pi\alpha_s c_{\gamma\gamma}^{(1)} \right), \tag{2.17}$$

where the functions $c_{\gamma\gamma}^{(0)}$ depend only on the ratio $\rho = s_{\gamma\gamma}/4m_Q^2$. These functions are shown in Fig. 2.9.

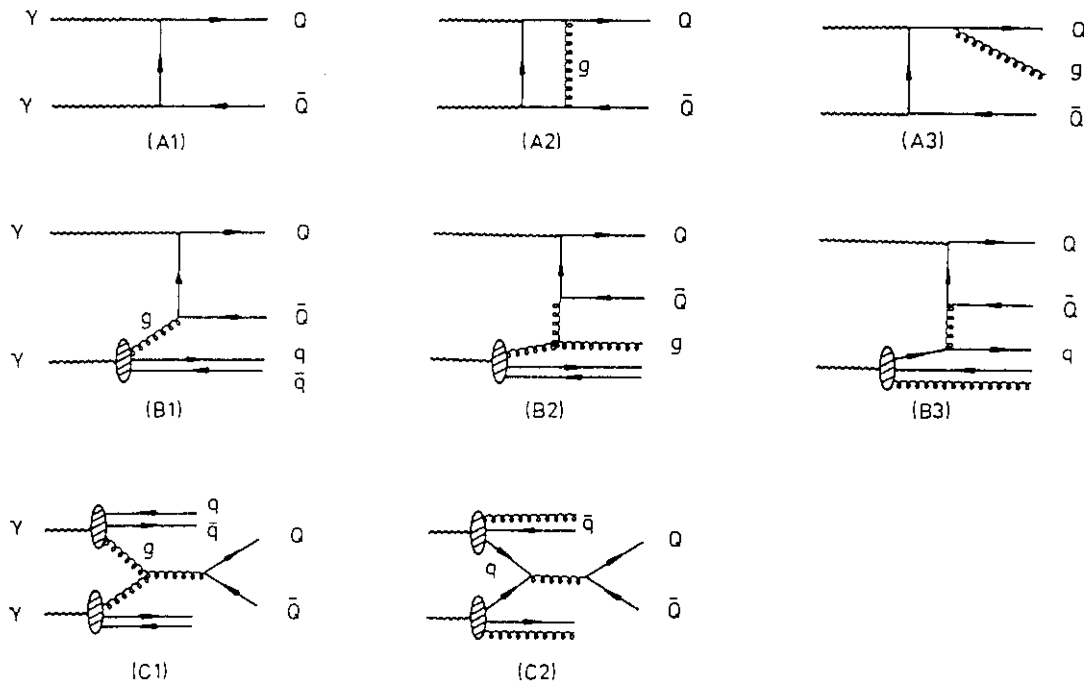

Figure 2.8: Generic diagrams for heavy-quark production in $\gamma\gamma$ collisions: (A) direct process, (B) one-resolved process, and (C) two-resolved process.

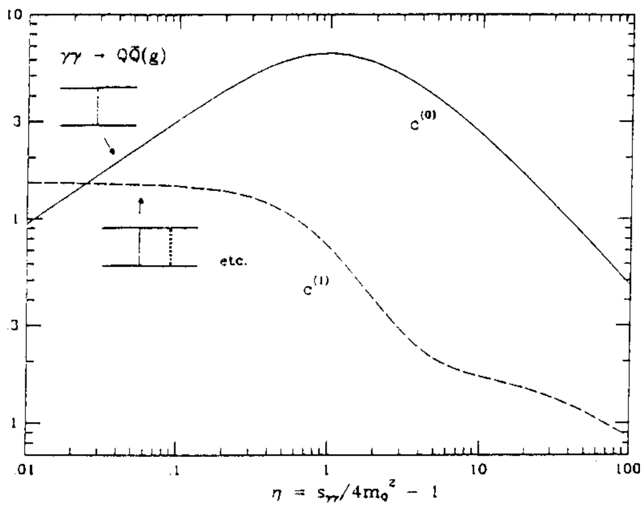

Figure 2.9: Coefficients of the QCD corrected total cross section for $\gamma\gamma \to Q\bar{Q}(g)$ in the physically relevant range of the scaling variable $s_{\gamma\gamma}/4m_Q^2$.

B. one-resolved process

The Born cross section for the one-resolved process (B1) can be derived from the equation2.15 by replacing $\alpha^2 e_Q^4 \rightarrow \frac{4}{3}\alpha\alpha_s e_Q^2$. As described earlier, the cross section for the resolved-photon process depends on the parton density in the photon. Since the parton density grows $\sim \alpha{\alpha_s}^{-1}$, the resolved photon process are the same order as the direct process. Besides the virtual QCD corrections and soft and hard gluon radiation (B2), the cross section in the next-to-leading order (NLO) involves also the subprocess of $\gamma g \rightarrow Q\bar{Q}q$ (B3). The QCD corrected cross sections of the subprocess are parametrized as

$$\sigma_{\gamma i} = \frac{\alpha\alpha_s e_Q^2}{m_Q^2}\left[c_{\gamma i}^{(0)} + 4\pi\alpha_s\left(c_{\gamma i}^{(1)} + \bar{c}_{\gamma i}^{(1)}\log\frac{\mu^2}{m_Q^2}\right)\right] (\mathrm{i = g, q,}), \tag{2.18}$$

where the coefficients $c_{\gamma g}$ and $c_{\gamma q} = \hat{c}_{\gamma q} + (e_q/e_Q)^2 d_{\gamma q}$ as functions of $s_{\gamma i}/4m_Q^2$ can be found in Ref.[14]; μ is the renormalization and factorization scale. In the $g\gamma$ subprocess, logarithmic singularities occur near threshold ($\beta \sim 0$) due to soft initial-state gluon radiation,

$$\sigma(\gamma g \rightarrow Q\bar{Q}(g)) = \frac{2\pi\alpha\alpha_s e_Q^2}{s_{\gamma g}}\beta\left[1 + \frac{\alpha_s}{\pi}\left(-\frac{1}{12}\frac{\pi^2}{\beta} + 3\log^2 8\beta^2 - 15\log 8\beta^2 - 3\log 4\beta^2 \log\frac{\mu^2}{m_Q^2} + O(\beta)\right)\right]. \tag{2.19}$$

Very close to the threshold, Sommerfeld's exponential suppression factor of $-(\pi\alpha_s/6\beta)[1 - exp(\pi\alpha_s/6\beta)]^{-1} \simeq -(\pi\alpha_s/6\beta)exp(\pi\alpha_s/6\beta)$[35] is lead by multiple gluon exchange.

For the parton densities in the photon, we have tried four typical parametrization given by DG[19], LAC1[13], and WHIT1,4[23] as working examples in this analysis.

C. Two-resolved process

The subprocess cross sections in the two-resolved process are given in Born approximation[36] by

$$\sigma(gg \rightarrow Q\bar{Q}) = \frac{\pi\alpha_s^2}{3s}\left[\left(1 + \frac{4m_Q^2}{s} + \frac{m_Q^2}{s^2}\right)\log\frac{1+\beta}{1-\beta} - \frac{\beta}{4}\left(7 + \frac{31m_Q^2}{s}\right)\right], \tag{2.20}$$

for (C1) and

$$\sigma(q\bar{q} \rightarrow Q\bar{Q}) = \frac{8\pi\alpha_s^2}{27s}\beta\left(1 + \frac{2m_Q^2}{s}\right), \tag{2.21}$$

for (C2). In the heavy-quark production, the two-resolved process contribution is much smaller than that of the direct and one-resolved process. Especially in the TRISTAN energy region, the contribution is considered to be negligible.

It is difficult to make an event generator including the NLO correction effect. We therefore considered the effect by calculating the k factor defined by $k = \sigma_{NLO}/\sigma_{LO}$ which characterizes the higher order corrections. We then multiply the factor to the various quantities in the Monte-Carlo simulation which carried out according to the LO cross section. In the Monte-Carlo simulation, string fragmentation which was used in hadronization process (described in Chapter 5) includes a parton-shower-like effect. The NLO correction in the P_T spectrum is therefore doubly counted. Instead, we used the P_T-independent correction to the direct process. The cross section for the direct process is increased by a factor of 1.31 uniformly. While that of the resolved-photon process is corrected by a P_T dependent function, due to the presence of the process $\gamma q \to c\bar{c}q$ (a part of this is absorbed in the gluon density function in the resolved photon). The obtained P_T^c-dependent correction was written as,

$$0.5P_T^c + 0.54,$$

where P_T^c was the P_T of the charm quark in GeV. Here the charm-quark mass (m_c) and the renormalization scale (μ) of 1.6 GeV and $\mu = \sqrt{m_c}$ were used, respectively[16].

Figs. 2.10 shows the differential cross sections of open-charm productions in two-photon processes with the current quark mass of (a) 1.5 GeV, and (b) 1.3 GeV, for P_T of the charm quark. Changing the current charm-quark mass of 1.5 GeV to 1.3 GeV, the total cross section increases about 30%. Figs. 2.10 also shows the difference between parametrization; Dashed line and solid one indicate the direct+DG and direct+LAC1, respectively. These two parametrization differ at low-x region. This difference reflects at low-P_T region, as shown in the figure. It is necessary to tag low-P_T c-quarks to study the difference between them.

So far c-quarks were tagged by D^* signals using the decay mode $D^* \to \pi_s D^0$ ($D^0 \to \pi K X$). However, because of the low Q-value in the reaction $D^* \to \pi_s D^0$, the momentum region of the reconstructed D^* is limited from the acceptance of the detected soft pion π_s. Therefore, it is difficult to tag low-P_T c-quarks by D^* method. On the other hand, using the decay mode $c \to e\nu X$, we can tag low-P_T c-quarks since the reaction has high Q-value.

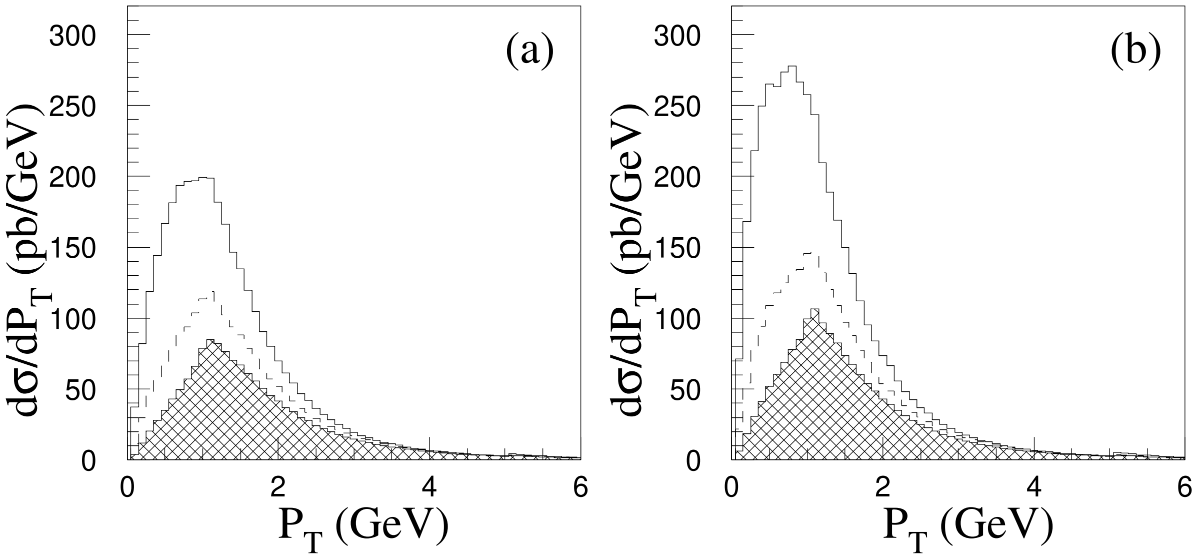

Figure 2.10: Differential cross section for charm-quark P_T. We set the current quark mass to be (a)1.5 GeV, and (b) 1.3 GeV. Hatched area describes the direct process only. Dashed and solid lines are the direct+ DG and direct + LAC1 predictions, respectively.